

© 2016 The Authors. Published by the British Institute of Radiology under the terms of the Creative Commons Attribution-NonCommercial 4.0 Unported License <http://creativecommons.org/licenses/by-nc/4.0/>, which permits unrestricted non-commercial reuse, provided the original author and source are credited.

## **A kernel-based dose calculation algorithm for kV photon beams with explicit handling of energy and material dependencies**

Anna Merle Reinhart, Martin F Fast, Peter Ziegenhein, Simeon Nill,  
and Uwe Oelfke

Joint Department of Physics at The Institute of Cancer Research and The  
Royal Marsden NHS Foundation Trust, London, UK SM2 5NG

**Short title:** A kernel-based kV dose engine

**Type of manuscript:** Full paper

**Acknowledgements:** Research at the ICR is also supported by Cancer Research UK under Programme C33589/A19727. MFF is supported by Cancer Research UK under Programme C33589/A19908.

# A kernel-based dose calculation algorithm for kV photon beams with explicit handling of energy and material dependencies

**Objectives:** Mimicking state-of-the-art patient radiotherapy with high precision irradiators for small animals is expected to advance the understanding of dose-effect relationships and radiobiology in general. We work on the implementation of intensity modulated radiotherapy-like irradiation schemes for small animals. As a first step we present a fast analytical dose calculation algorithm for keV photon beams.

**Methods:** We follow a superposition-convolution approach adapted to kV x-rays, based on previous work for microbeam therapy. We assume local energy deposition at the photon interaction point, due to the short electron ranges in tissue. This allows us to separate the dose calculation into locally absorbed primary dose and the scatter contribution, calculated in a point kernel approach. We validate our dose model against Geant4 Monte Carlo simulations, and compare the results to Muriplan (XStrahl Ltd, Camberley, UK).

**Results:** For field sizes of 1 mm to 1 cm in water, the depth dose curves show a mean disagreement of 1.7% to Monte Carlo simulations, with the largest deviations in the entrance region (4%) and at large depths (5% at 7 cm). Larger discrepancies are observed at water-to-bone boundaries, in bone and at the beam edges in slab phantoms and a mouse brain. Calculation times are in the order of 5s for a single beam.

**Conclusions:** The algorithm shows good agreement with Monte Carlo simulations in an initial validation. It has the potential to become an alternative to full Monte Carlo dose calculation.

**Advances in knowledge:** The presented algorithm demonstrates the potential of kernel-based dose calculation for kV photon beams. It will be valuable in IMRT and inverse treatment planning for high precision small animal radiotherapy.

## I. INTRODUCTION

Mimicking the spatial and temporal dose distributions delivered in state-of-the-art patient treatment in a pre-clinical setting is expected to advance dose-effect studies and radiobiological investigations.<sup>1</sup> To this effect, a number of research groups have developed precision radiotherapy systems for small animals.<sup>2-7</sup> In contrast to conventional pre-clinical irradiations, these systems allow positioning and irradiation of tissues of interest with sub-millimetre accuracy. Common features of high precision irradiation devices consist of a 225kVp x-ray tube mounted on a rotating gantry, a precise collimation system down to 0.5mm beam size, a robotic couch as well as on-board cone-beam computed tomography (CBCT) and planar imaging.

From a hardware point of view, these irradiators are capable of delivering complex dose distributions. However, sophisticated dose calculation and treatment planning systems (TPS) are still required to fully exploit their potential.<sup>8</sup> Clinically available tools designed for patient treatment are not suitable for small animal radiotherapy, due to the different energy regime (kV instead of MV) and much smaller field sizes.<sup>9</sup> In addition, the workflow in pre-clinical irradiations differs from patient treatment. The anaesthetised animal is imaged, planned, and treated subsequently in one anaesthesia setting of approximately 15 minutes, which requires especially short treatment planning times.

The introduction of pre-clinical precision irradiators has sparked the development of dedicated dose calculation methods for treatment planning tools.<sup>9</sup> Different approaches

1 were pursued, from a measurement-based method<sup>10</sup> and a superposition-convolution  
 2 algorithm<sup>11-13</sup> to Monte Carlo-based dose calculation algorithms.<sup>14-16</sup> The available  
 3 planning tools for pre-clinical radiotherapy currently support forward-planned dose  
 4 delivery techniques with open treatment fields from multiple beam directions or arcs,  
 5 with the recent addition of beam-on time optimization.<sup>17</sup>

6 We intend to further advance pre-clinical radiotherapy by developing intensity  
 7 modulated dose delivery techniques based on inverse planning strategies. The small  
 8 animal specific workflow combined with inverse optimization requires an accurate and  
 9 fast dose calculation. While Monte-Carlo-based dose calculation algorithms are the gold  
 10 standard in terms of accuracy, they generally suffer from long calculation times. Kernel-  
 11 based methods permit fast dose calculations, but introduce inherent uncertainties at  
 12 tissue boundaries, and care has to be taken to correctly model the kV photon  
 13 interactions with matter. In this work, we present a superposition-convolution dose  
 14 engine, with explicit handling of energy and material dependencies.  
 15

## 16 17 18 II. MATERIALS AND METHODS

### 19 20 A. Dose calculation

21  
22  
23 When comparing photon beam interactions of kV and MV energy spectra three main  
 24 differences have to be accounted for. First, the importance of the photo-electric effect for  
 25 kV energies is increased. The cross-section of the photo-electric effect scales with the  
 26 atomic number as  $Z^{3-4}$ , introducing a strong material dependence of the absorption  
 27 coefficients. Therefore, knowledge of the electron density alone is no longer sufficient,  
 28 but information on the tissue composition is also required. Additionally, the cross-  
 29 section depends strongly on the photon energy. Second, the angular distribution of the  
 30 differential cross section for Compton scattering changes. Instead of being strongly  
 31 forward-peaked, the angular distribution of scattering angles is more isotropic. Finally,  
 32 the range of secondary electrons in water is much shorter for kV energies, in the order  
 33 of a few  $\mu\text{m}$  to a few hundred  $\mu\text{m}$ . Thus, energy is transported through matter by  
 34 scattered photons, rather than secondary electrons, and the build-up effect is small.  
 35

36 These peculiarities have to be accounted for and modelled in any dose calculation  
 37 algorithm for kV photons. Our approach to do so is based on a superposition-  
 38 convolution algorithm. Superposition-convolution is a two-step process. First, the local  
 39 photon fluence at any point  $\vec{x}$  is determined via the total energy released per unit mass  
 40 (TERMA)  
 41

$$42 \text{TERMA}(\vec{x}, E) = \phi_0 E \frac{\mu(\vec{x}, E)}{\rho_{mass}} \exp \left[ - \int_{\gamma} \mu(\gamma(s), E) ds \right], \quad (1)$$

43  
44 with the initial photon fluence  $\phi_0$ , the energy  $E$ , the attenuation coefficient  $\mu$ , the mass  
 45 density  $\rho_{mass}$  and the path of the photons  $\gamma$ . The dose is then calculated as a convolution  
 46 of the TERMA with a dose deposition kernel.  
 47

#### 48 49 50 51 52 53 1. Dose model

54  
55 Our dose model is based on previous work on microbeam radiation therapy  
 56 (MRT).<sup>18,19</sup> In MRT targets are irradiated with parallel kV photon microbeams with a  
 57 width of a few micrometres. In this approach,<sup>18</sup> interactions of photons and electrons  
 58 with matter are treated separately due to their different ranges in tissue. The dose  
 59 deposition kernel is split into a photon kernel and an electron kernel. For small animal  
 60  
 61  
 62  
 63  
 64  
 65

1 radiotherapy, this can be further simplified. Electrons with an energy of 80keV, the  
 2 mean energy of the commercially available systems, have a range of approximately  
 3 100 $\mu$ m in water. This is of the same order of magnitude as the voxel size. We therefore  
 4 assume local energy deposition at the primary photon interaction site.

5 For simplicity, we briefly describe the algorithm assuming monoenergetic beams in  
 6 homogeneous media. The dose deposition kernel can be separated into energy  
 7 deposited locally by the primary interaction and a scatter kernel. At the primary  
 8 interaction point, the average fraction  
 9

$$10 \quad f_E = q_P + q_C \cdot p_C = (1 - q_C - q_R) + q_C \cdot p_C \quad (2)$$

11 of the photon energy is transferred to the medium.<sup>19</sup>  $q_P$ ,  $q_C$  and  $q_R$  denote the  
 12 probabilities for the photo-electric effect, Compton and Rayleigh scattering respectively,  
 13 defined as the ratio of absorption coefficients  $\mu$ ,  $q_{\text{interaction}} = \mu_{\text{interaction}}/\mu_{\text{total}}$ .  $p_C$  is the  
 14 energy fraction transferred to Compton electrons.<sup>19</sup> The primary dose can thus be  
 15 expressed as  
 16  
 17  
 18

$$19 \quad D_{\text{primary}}(\vec{x}) = f_E \cdot \text{TERMA}(\vec{x}). \quad (3)$$

20 All further energy deposition by scattered particles is treated in a point kernel approach.  
 21 The scatter dose contribution is calculated as a convolution of TERMA with a pre-  
 22 calculated dose deposition kernel (c.f. section II A 3)  
 23  
 24  
 25

$$26 \quad D_{\text{scatter}}(\vec{x}) = \text{Kernel} * \text{TERMA}(\vec{x}). \quad (4)$$

27 The total dose deposited is the sum of primary and scatter contributions  $D_{\text{total}} =$   
 28  $D_{\text{primary}} + D_{\text{scatter}}$ .

29 To account for the energy and material dependencies of the absorbed dose, the  
 30 calculations outlined above are performed for a discrete set of monoenergetic photons  
 31 and homogeneous materials. The absorbed dose in inhomogeneous media irradiated by  
 32 polychromatic beams is calculated as an energy-weighted sum of these contributions:  
 33  
 34  
 35

$$36 \quad D(\vec{x}) = \sum_E^{N_E} w_E \left[ f_E \cdot \text{TERMA}(\vec{x}, E) + \sum_M^{N_M} (\text{Kernel}(E, M) * \text{TERMA}(\vec{x}, E, M)) \right], \quad (5)$$

37 where  $w_E$  is the weight of the energy bin in the spectrum with  $\sum w_E = 1$ , and  $N_E$  and  $N_M$   
 38 are the numbers of energy and material components.  
 39  
 40  
 41  
 42  
 43  
 44  
 45  
 46  
 47  
 48

## 49 *2. Handling of energy and material dependencies*

50 As discussed in section II A 1, the dose is calculated as a weighted sum of discrete energy  
 51 and material contributions. The number of chosen calculation points balances accuracy  
 52 and runtime. We currently employ 6 photon energies and 10 different materials.

53 The energy sampling points are spaced equally in the cumulative energy-weighted  
 54 spectrum. The weights  $w_E$  are given by the spectral integral of the energy bin and satisfy  
 55  $\sum w_E = 1$ . The energy values and respective weights for the small animal radiation  
 56 research platform (SARRP, XStrahl Ltd., Camberley, UK) are given in table I.

57 The dose calculation requires knowledge of the absorption coefficients of the  
 58 irradiated materials, which depend on the tissue composition in addition to the density  
 59 for kV dose calculation. The tissue parameters are extracted from the Hounsfield units  
 60  
 61  
 62  
 63  
 64  
 65

TABLE I: Sampling points of the energy spectrum and their respective weighting factors

$w_E$ .						
<b>E [keV]</b>	45	60	80	105	130	170
<b><math>w_E</math></b>	0.2004	0.3811	0.1344	0.1097	0.0950	0.0794

TABLE II: List of materials for which the scatter dose kernels are pre-calculated. The density  $\rho$  is given in  $\text{gcm}^{-3}$ , and the elemental weights  $w_i$  are weight fractions in %.

<b>M</b>	<b>HU</b>	<b><math>\rho</math></b>	<b><math>w_H</math></b>	<b><math>w_C</math></b>	<b><math>w_N</math></b>	<b><math>w_O</math></b>	<b><math>w_P</math></b>	<b><math>w_{Ca}</math></b>
1	-700	0.31	3.86	22.65	50.46	22.00	0	0
2	-350	0.67	8.36	49.07	21.24	20.72	0	0
3	-99	0.93	11.59	68.02	0.28	19.80	0	0
4	99	1.12	9.41	20.59	6.15	62.35	0	0
5	408	1.26	7.77	37.00	2.99	37.75	4.44	9.57
6	617	1.38	6.63	31.40	3.31	39.25	5.96	12.94
7	779	1.48	5.88	27.71	3.51	40.24	6.97	15.16
8	1038	1.63	4.87	22.71	3.80	41.57	8.33	18.16
9	1167	1.71	4.43	20.56	3.92	42.15	8.92	19.46
10	1416	1.86	3.69	16.19	4.12	43.12	9.92	21.65

(HU) of the CT according to the method described by Schneider et al.<sup>20</sup> It has to be noted that the tissue parameters are based on human tissues, since very limited data on small animal tissue compositions is available. These continuous tissue parameters are directly used in the calculation of the TERMA and the primary dose through analytical approximations of the absorption coefficients.<sup>18,19</sup>

The scatter dose, on the other hand, is calculated for a set of 10 materials. For each voxel, we determine the base material closest to the voxel material, and use the appropriate kernel in the convolution. The 10 base materials are given in table II. They do not correspond to common tissues, but are chosen heuristically based on the absorption coefficients, as follows: The material-dependent part of the absorption coefficient for the photo-electric effect has an approximately exponential relationship to that of the Compton scattering. In order to limit the variation in both absorption coefficients within each material segment and thus limit the dose calculation error, we therefore use an exponential segmentation

$$M(F_1) = \lfloor e^{\alpha \cdot F_1} \rfloor, \quad (6)$$

where  $\alpha = 2.5\text{cm}^3\text{g}^{-1}$ . Each material is assigned to a material segment  $M \in \{1, 2, \dots, 10\}$  based on the material dependent part of  $\mu_c$ :

$$F_1 = \sum_i N_A w_i \frac{Z_i}{A_i} \rho, \quad (7)$$

with the Avogadro constant  $N_A$ , the elemental weights  $w_i$ , the atomic number and mass  $Z_i$  and  $A_i$ , and the mass density  $\rho$ .

### 3. Kernels

We generated the scatter dose deposition kernels with the Monte Carlo engine Geant4<sup>21,22</sup> version 10.01p01, using the PENELOPE electro-magnetic physics list. For all 60 energy and material combinations,  $5 \cdot 10^8$  to  $10^9$  particle histories were simulated in homogeneous cubes with mono-energetic photon beams. A biasing region of  $\frac{1}{8}$  of the voxel size was defined at the centre of the cube, and a mono-energetic, uni-directional photon point source was placed on the border of this region. All primary photons were forced to interact within this biasing region. The dose was scored into a cube with  $251^3$  cubic voxels with a size of  $(0.275\mu\text{m})^3$ . Energy deposited by secondary electrons originating from the first interaction was not scored, as this is accounted for in the primary dose.

The geometry of the pre-clinical irradiators, combined with the small treatment fields used in small animal radiotherapy, leads to small beam divergences. For the SARRP system, the maximal beam divergence of a  $1\text{cm}^2$  field is  $1.15^\circ$ . In addition, the angular dependence of the Compton scattering cross section leads to almost isotropic scatter kernels. We therefore neglect the beam divergence within a single beam. An exploratory analysis showed that even with kernels tilted by  $45^\circ$  against the beam direction, the errors in the dose distribution are small. For example, for a  $5\text{mm} \times 5\text{mm}$  irradiation field in water, a rotation of the kernels by  $45^\circ$  led to local deviations below 0.5% in both the depth dose curve and the lateral profile. Therefore, we do not rotate the kernels to the beam direction. Instead, we determine the main axis closest to the beam direction and flip the kernel by  $0^\circ$ ,  $90^\circ$ ,  $180^\circ$  or  $270^\circ$  accordingly. The TERMA for all beams within a quadrant is summed, and the scatter dose calculated once for each quadrant. This reduces the number of convolutions from  $N_{\text{beam}} \times 60$  to a maximum of  $4 \times 60$ . This enables the calculation of complex dose deliveries such as many-beam treatments or deliveries with a variable collimator, and we do not foresee any issues with the implementation of conformal arcs in the future.

### 4. Implementation

In order to evaluate the performance of the algorithm, we developed a basic stand-alone TPS, which calculates the dose for a given CT and treatment plan as illustrated in figure 1.

In a first step, the CT Hounsfield Units (HU) are converted to material properties (see II A 2). The TERMA is pre-calculated for all beams and energy contributions using a Siddon raytracer,<sup>23</sup> which calculates the photon attenuation in depth by raytracing from a point source to a grid of target points behind the CT volume.<sup>24</sup> The actual dose calculation is then split into primary and scattered dose as described above.

Currently, the dose engine is adapted to the geometry of the SARRP. In our current implementation we only account for the primary radiation emerging from the focal spot of the radiation source but neglect scatter or leakage radiation from the collimator, similar to the approach described by Granton et al.<sup>25</sup> The 3mm focal spot is approximated by a 2D Gaussian distribution.

The cross-platform compatible implementation of the dose calculation method runs on a multi-core CPU environment. All modules of the software have been implemented for modern parallel processors. The convolutions of TERMA and kernel for all energy and material combinations are calculated in Fourier space, and implemented using the fast Fourier transformations of the Intel mkl library.<sup>26</sup> To prevent cross correlations due to circular convolution of non-periodic signals in Fourier space the input is typically zero-padded by the size of the kernel. However, this increases the size of the convolution problem and hence the calculation time significantly. The sharp fall-off of the kV dose kernels limits the aliasing errors on the dose distribution. We therefore reduced the zero-padding to half the size of the kernels.

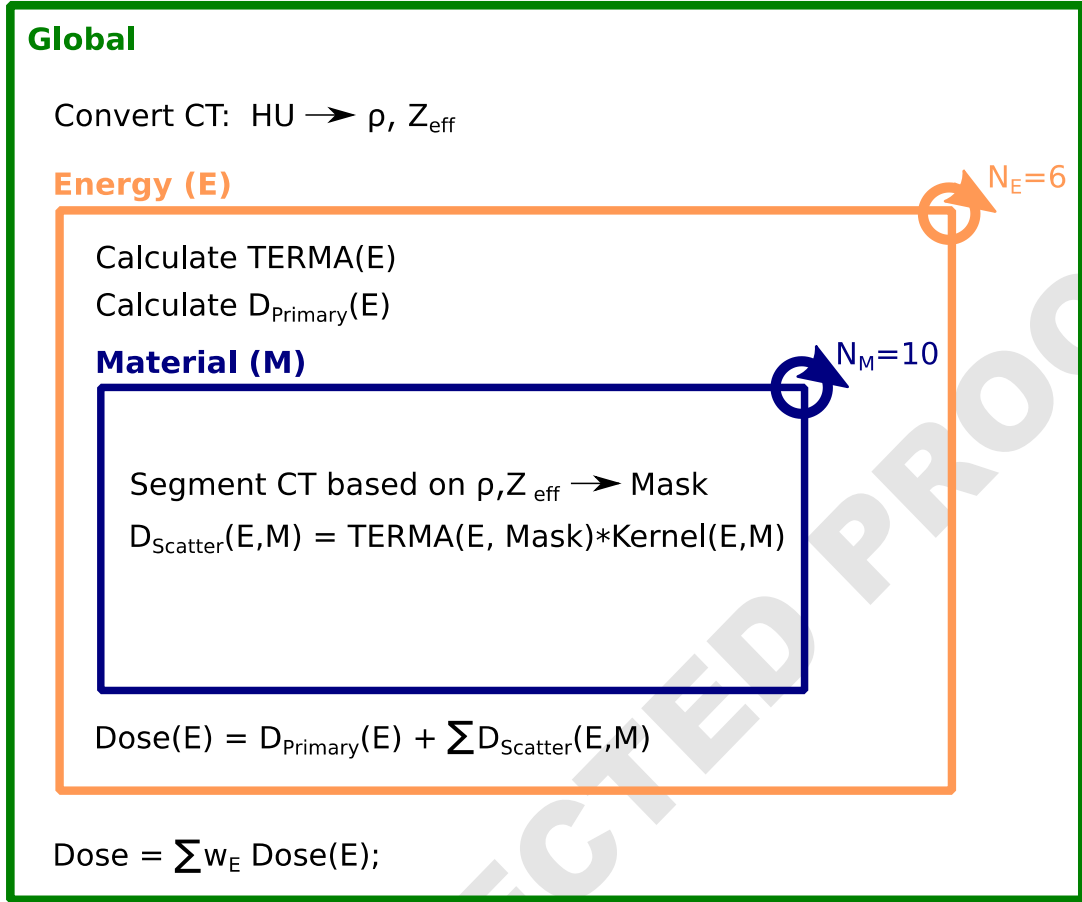


FIG. 1: Workflow of the developed dose calculation algorithm.

### B. Monte Carlo reference dose

Monte Carlo simulations are generally accepted as the gold standard in terms of accurate dose calculation. We therefore compared our dose engine with Monte Carlo simulations to validate the calculation accuracy. As for the kernel calculation (c.f. IIA3), we used the Geant4 toolkit v10.01p01,<sup>21,22</sup> with the PENELOPE electro-magnetic physics description. The same simplified geometry of the SARRP system used in the superposition-convolution dose engine is implemented. The photon energy is sampled from the spectrum, without the discretisation needed in the presented dose engine. The same beam parameters are used as input for the simulation and our kernel-based dose calculation, and the conversion method of HUs to material properties are identical.

### C. Muriplan

In addition to MC simulations, we compared our dose engine to Muriplan 2.0.1 (XStrahl Ltd., Camberley, UK), the treatment planning system supplied with the SARRP. Muriplan was developed at Johns Hopkins University, Baltimore. It uses a superposition-convolution dose engine implemented on a GPU, based on their MV dose calculation algorithm.<sup>11-13</sup> The entire small animal treatment is controlled from its 3DSlicer<sup>27</sup>-based user interface.<sup>28</sup> The acquired CBCT is transformed into material properties by defining 5 discrete windows for the materials air, lung, fat, tissue and bone. For phantom

1 experiments, presets for air, cork, water, graphite and aluminium are available. The dose  
2 engine uses look-up tables for the absorption coefficients of these materials, according  
3 to the NIST database.<sup>29</sup> The tissue density and tissue composition are taken from the  
4 ICRU Report 44.<sup>30,31</sup> The energy dependence is integrated into the TERMA calculations,  
5 using 21 energy bins.<sup>11</sup> During the installation of the SARRP system on site, Muriplan is  
6 commissioned using measurement data. To the best of our knowledge no detailed  
7 information on the performance of Muriplan or the dose engine has been published.  
8  
9

#### 10 D. Validation

11  
12 We validated our developed dose calculation software by comparison to Geant4  
13 Monte Carlo simulations (c.f. II B) and compared it to the commercial treatment  
14 planning system Muriplan (c.f. II C). We evaluated the dose distributions in a virtual  
15 homogeneous water phantom, virtual slab phantoms of soft tissue with bone and lung  
16 inserts, as well as those calculated on a mouse CBCT. The voxel size was  $(0.275\text{mm})^3$ ,  
17 the standard voxel size at the SARRP. The dose is reported as dose to medium in all  
18 cases.  
19

20 First, we demonstrate the performance of the new dose engine in a  $(7.04\text{cm})^3$   
21 homogeneous water phantom for three different square treatment fields of  $(1\text{mm})^2$ ,  
22  $(5\text{mm})^2$ , and  $(10\text{mm})^2$ . In order to evaluate the performance in inhomogeneous  
23 materials, we inserted a 2mm bone slab or a 5mm lung slab into a soft tissue phantom,  
24 positioning the top of the slab at a depth of 5mm. In both cases, we used a  $(5\text{mm})^2$   
25 square treatment beam.  
26

27 For our dose comparison we created virtual CT cubes with  $(256)^3$  voxels. The HU-  
28 tissue association as described by Schneider et al.<sup>20</sup> resulted in  $\text{HU}_{\text{water}}=0$ ,  $\text{HU}_{\text{softtissue}}=43$ ,  
29  $\text{HU}_{\text{lung}}=-741$  or  $\text{HU}_{\text{bone}}=1542$  for the ICRU-44 materials used in Muriplan. The same CTs  
30 were imported into Muriplan, and the materials assigned accordingly. In the MC  
31 simulations, we created the virtual phantom directly in Geant4 from the material  
32 compositions.  
33

34 Finally, we calculated the dose distributions on a mouse CBCT acquired at the SARRP.  
35 It has to be noted that the output of the on-board CBCT of the SARRP are not Hounsfield  
36 units but arbitrary units, as the system is not calibrated for absolute attenuation  
37 coefficients. Therefore, the uncalibrated CT numbers of the mouse CBCT were converted  
38 to HUs prior to the dose calculation using piece-wise linear interpolations between the 5  
39 materials used in Muriplan. The converted CT was used in the new dose engine as well  
40 as in the MC simulations. In Muriplan the standard 5 material workflow was used. We  
41 defined an artificial target in the mouse brain, and planned a 5-field irradiation with  
42 equidistant beams of  $3\text{mm} \times 3\text{mm}$  at  $0^\circ$ ,  $72^\circ$ ,  $144^\circ$ ,  $216^\circ$  and  $288^\circ$ .  
43

44 The runtime of our dose calculation method was measured on a shared memory  
45 system configured with two Intel Xeon E5-2697v3 CPUs.  
46  
47

### 48 III. RESULTS

#### 49 A. Dose distributions

##### 50 1. Phantoms

51  
52 The dose distributions in water calculated with our kernel-based algorithm,  
53 Muriplan, and MC simulations are compared in figure 2. For three different treatment  
54 field sizes ( $(1\text{mm})^2$ ,  $(5\text{mm})^2$ , and  $(10\text{mm})^2$ ), the depth dose curves as well as the lateral  
55 profiles at a depth of 6mm are shown. Both our kernel-based algorithm and the MC  
56 simulations have not yet been calibrated in terms of machine output and therefore no  
57  
58  
59  
60  
61  
62  
63  
64  
65



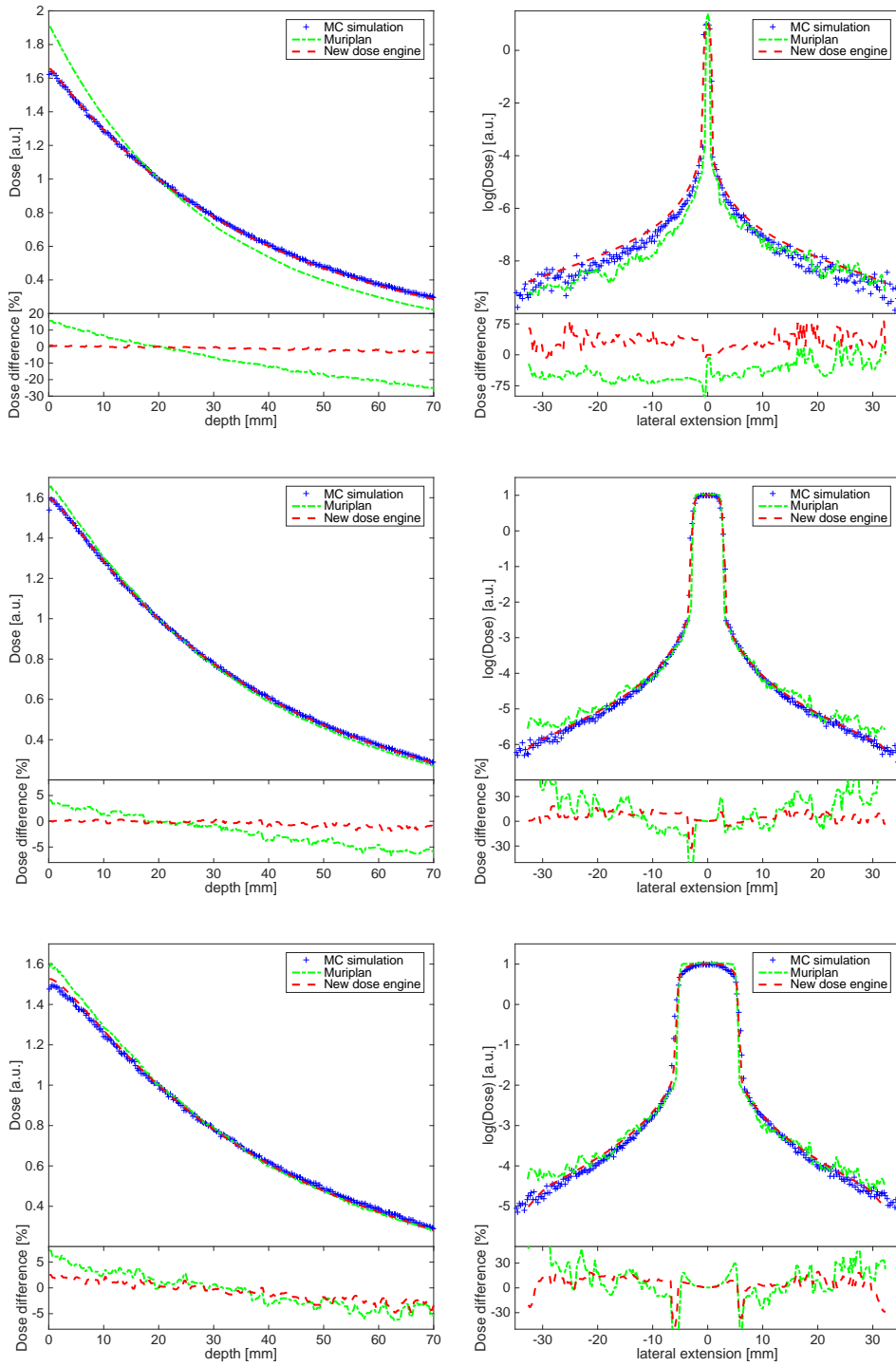


FIG. 2: Comparison of the analytical dose engine with Muriplan and MC simulations in water. Depth dose curves (left column) and lateral profiles at a depth of 6mm (right column) are shown for three different field sizes ( $(1\text{mm})^2$  top row,  $(5\text{mm})^2$  middle row, and  $(10\text{mm})^2$  bottom row). The depth dose curves are normalized to the value at 2cm depth. The local percentage differences were smoothed with a 3-median filter to reduce the visual impact of MC noise.

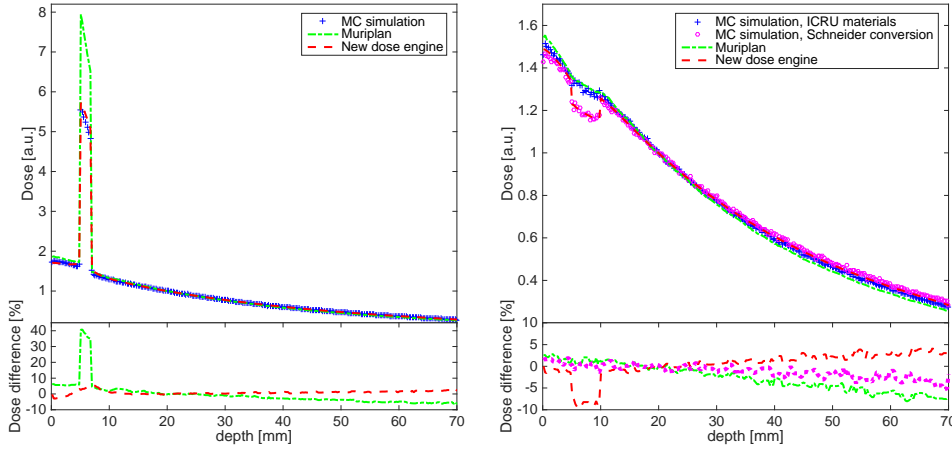


FIG. 3: Comparison of the depth dose curves of  $(5\text{mm})^2$  fields, normalized to the value at 2cm depth, calculated with the analytical dose engine, Muriplan, and MC simulations in slab phantoms of soft tissue with bone (left) and lung (right) inserts. The local percentage differences, smoothed with a 3-median filter, are shown in the bottom row.

direct correlation between delivery times and absolute dose is possible. Therefore, the depth dose curves are normalised to the point at 2cm depth, as this is the standard reference point in kV dosimetry protocols. The lateral profiles are normalized to the integral of the depth dose curve.

For our dose engine (shown in red), the mean agreement of the calculated depth dose curves with the simulations is 1.7% for all collimator sizes in water. Larger deviations of up to 4% are observed in the first voxel, i.e. in a 0.275mm deep entrance region. In addition, the deviation between the new analytical algorithm and MC simulations increases with depth, but does not exceed 5%. The lateral beam profiles were evaluated at different depths (a depth of 6mm was chosen for demonstration purposes in figure 2). Within the beam, the simulations and our superposition-convolution algorithm show a mean agreement of 3% for all beams, apart from the beam edge. The out-of-field doses, which are defined by values smaller than 10% of the maximum dose, agree within 12% (mean) for the  $(5\text{mm})^2$  and  $(10\text{mm})^2$  beams, up to a distance of 34mm, which corresponds to the size of the kernel. For the smallest treatment field, the mean agreement is 22%.

The depth dose curves calculated with Muriplan (shown in green) agree with the simulations within 3% (mean) for the  $(5\text{mm})^2$  and  $(10\text{mm})^2$  beams, and 12% (mean) for the smallest field. The dose fall-off is consistently steeper in Muriplan compared to the MC simulations, and this effect is most pronounced for the smallest beam size. In the lateral profiles, the mean agreement is 3% within the beam and 20% (mean) in the out-of-field regions for all but the smallest fields. For the  $(1\text{mm})^2$  field, the in-beam region agrees within 11%, and the out-of-field doses to 43% (mean). It has to be noted, however, that a different head model is used in the MC simulations and Muriplan, which probably accounts for the large differences in the smallest field size.

Figure 3 depicts the depth dose curves in slab phantoms of water with either 2mm of bone or 5mm of lung inserted at a depth of 5mm. For the new dose engine, the mean agreement in the bone case is 1.5%, with the largest deviations up to 7% at the boundary of the bone slab.

In Muriplan, the dose in the bone insert is overestimated by up to 43% compared to the MC simulations. For the lung phantom, simulations and the Muriplan results agree within 3% (mean), while our analytical calculations underestimate the dose in lung by 9%. However, if the same CT and material conversion as in the analytical dose

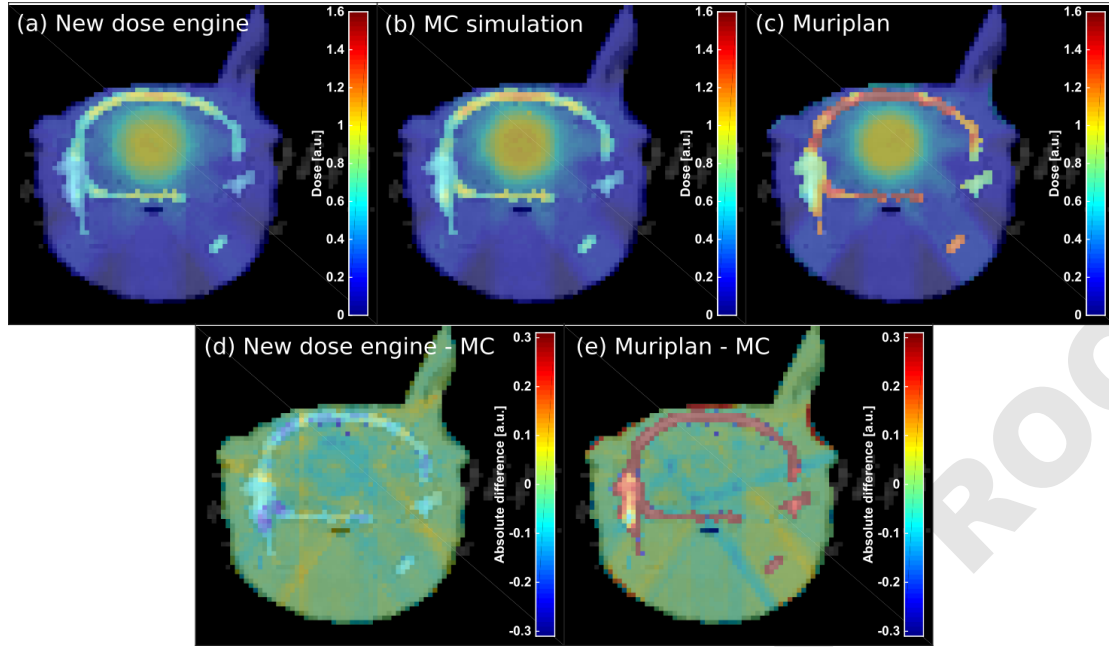


FIG. 4: Dose distributions from a five  $(3\text{mm})^2$  field irradiation calculated on a mouse CBCT using the new dose engine (a), MC simulations (b) and Muriplan (c). The absolute dose differences are shown in the bottom row.

calculation are used in the MC simulation (Schneider conversion, shown in pink), our new dose engine and simulations agree within 2% (mean). The same tendencies regarding the build-up region, larger depths and the slope of the depth dose curves as in the water phantoms are observed in the slab phantoms.

## 2. Mouse CBCT

The dose distributions from a five-field irradiation of a mouse brain, obtained with our kernel-based dose engine, MC simulations, and Muriplan are shown in figure 4(a), 4(b), and 4(c), respectively. They are normalized to the dose at the centre of the target. The MC simulations were calculated to a statistical uncertainty of 0.5% in the target region. In the bottom row of figure 4, the dose difference maps between the simulated dose distribution and our dose engine (fig. 4(d)) and Muriplan (fig. 4(e)) are shown. In both cases, the largest differences can be observed in bone and at the beam edges. Muriplan overestimates the dose in bone by 53% (mean), while our dose engine shows an underdose of 14% (mean).

## B. Calculation times

The calculation times depend on the size of the CT and the number of treatment beams. In our implementation the calculation time does not change significantly from 4 beams onwards, since we perform the scatter dose calculation for four quadrants instead of each beam. As described in section II A 4, we reduced the zero-padding of the scatter dose kernels to reduce the runtime. We found that this influences the results by less than  $10^{-4}\%$ , while saving roughly 40% of the calculation time. The calculation times of the single-beam plans on the cubic water CT with  $(256)^3$  voxels and the five-beam plan on the mouse CT are given in table III.

TABLE III: Calculation times for different CT and beam configurations for our dose engine (using loss-less full padding and the reduced padding approximation) and Muriplan.

Test case	Mean calculation time [s]		
	New dose engine		Muriplan
	Full padding	Half padding	
256 <sup>3</sup> water cube, (1mm) <sup>2</sup> beam	8.03 ± 0.19	4.09 ± 0.03	5.53 ± 0.03
256 <sup>3</sup> water cube, (5mm) <sup>2</sup> beam	9.91 ± 0.19	5.16 ± 0.20	5.43 ± 0.15
256 <sup>3</sup> water cube, (10mm) <sup>2</sup> beam	11.97 ± 0.15	7.89 ± 0.09	5.50 ± 0.15
128 <sup>2</sup> × 326 mouse CBCT, 5 (3mm) <sup>2</sup> beams	31.54 ± 0.26	18.03 ± 0.25	18.37 ± 0.19

#### IV. DISCUSSION

In this study, we presented a superposition-convolution-based dose engine for small animal radiotherapy. Due to the fact that pre-clinical irradiators operate in the kV energy regime instead of MV, the increased importance of the photo-electric effect and the resulting increased material and energy dependencies have to be taken into account<sup>32</sup>. We split the calculation into energy deposited by the primary interaction and all subsequent scattering events. The primary dose is calculated analytically based on statistical considerations. The scatter dose is calculated as a convolution of TERMA with the appropriate MC-generated kernel from a set of 60 energy and material combinations.

We implemented the algorithm into a basic stand-alone TPS. The cross-platform compatible software is optimised for modern multi-core CPU systems. It has been adapted to the geometry and energy spectrum of the SARRP system, but can be adapted to any pre-clinical irradiator.

In comparisons with MC simulations, the depth dose curves in water show a mean disagreement of 1.7% (c.f. figure 2). A larger deviation of up to 4% is observed in the first voxel. This behaviour is expected, since the kernel-based approach does not correctly model the build-up effect, and overestimates the dose in the entrance region. For the energies used in pre-clinical research, the electron ranges and hence the build-up region are of the same order of magnitude as the voxel size.

One factor causing the increasing deviation in depth is our energy sampling approach. As discussed in section II A 2, the TERMA and hence the attenuation in depth is calculated separately for each of the 6 energy contributions. Beam hardening is therefore implicitly accounted for. However, we only regard 6 discrete energy values, and a careful analysis of the chosen sampling points could further improve the calculations. In the lateral profiles, large deviations at the field edge can be observed. This is a discretisation effect of the raytracing through a voxelised geometry. The out-of-field dose values agree within 12% for all but the smallest beam. Improving the dose calculation accuracy at the beam edges is expected to also increase accuracy distant from the beam. This issue will be addressed in future work.

The dose distributions in water calculated with Muriplan show systematic differences to our MC simulations. It has to be noted that, in contrast to the MC simulations and our dose engine, Muriplan has been commissioned to measurements. The differences in slope of the depth dose curves are most pronounced for the 1mm field. We assume this is due to differences in the head model. For the smallest beam sizes, the focal spot distribution becomes important<sup>33</sup>. This highlights the importance of

1 a thorough validation of the treatment dose calculation by comparison to  
2 measurements, especially for the smallest beam sizes. Future work includes the  
3 commissioning of our dose engine and an adaption of the head model where necessary.

4 In the slab phantoms, larger deviations between our dose calculation and MC  
5 simulations are observed at tissue interfaces (c.f. figure 3). This is an inherent issue of  
6 kernel-based approaches. Our approach of choosing the appropriate kernel for each  
7 voxel based on the voxel material assumes local homogeneity. Kernel stretching is not  
8 straightforwardly adapted from MV dose calculations to the kV energy regime, due to  
9 the increased importance of the photo-electric effect. This results in a smearing of the  
10 scatter dose at sharp tissue boundaries. The primary dose is not affected since there is  
11 no material approximation in its calculation.

12 In addition, discrepancies are observed within the tissue slabs. In bone, Muriplan  
13 overestimates the dose by up to 43%, while our dose engine underestimates dose to  
14 lung by up to 9%. In these cases, we used the ICRU material definitions of the Muriplan  
15 base materials in the MC simulations. Our dose engine, however, transforms HUs to  
16 material parameters according to Schneider et al.<sup>20</sup> If the same CT and material  
17 conversion as in the analytical dose calculation are used in the MC simulation, the mean  
18 disagreement in lung reduces to 2%. The overestimation in bone observed with  
19 Muriplan however cannot be explained by the tissue segmentation. In Muriplan, the  
20 kernels are calculated in water and the dose-to-water is converted to dose-to-medium  
21 using the ratio of mass energy absorption coefficients in water and tissue.<sup>34</sup> While this  
22 approach is suitable in MV dose calculations, it introduces errors in the kV energy  
23 regime which will be resolved in the future using correction factors for dose-to-  
24 medium.<sup>34</sup>

25 The same tendencies as in the water and slab phantoms can be observed in the 5-  
26 field irradiation of a mouse brain (c.f. figure 4). Discrepancies between MC and  
27 analytically calculated dose distributions are largest within bone, at the beam edges and  
28 tissue-bone interfaces.

29 The deviations introduced by the material segmentation are not surprising. Bazalova  
30 et al.<sup>32</sup> suggest that 29 materials are needed to calculate the dose to within 2 % for  
31 225kV photon beams on noisy CT images. A 4-tissue segmentation similar to the one  
32 used in Muriplan lead to dose differences of 57% in the ribs<sup>32</sup>, which, in combination  
33 with the discrepancies in the bone slab described above, corresponds well to the  
34 overestimation of dose in bone we observe in the skull for Muriplan. Using 8 tissues in  
35 the segmentation leads to errors in the order of 7%.<sup>32</sup> We currently use 10 base  
36 materials for the scatter dose kernels as a compromise between calculation time and  
37 accuracy. However, this segmentation does not affect the primary dose calculation  
38 where we calculate the absorption coefficients for each voxel based on the local material  
39 parameters (c.f. A II 2). This reduces the influence of the material segmentation on the  
40 dose distributions, but requires accurate material definitions. The discrepancies  
41 between the doses in lung calculated with different material definitions suggest that  
42 improvements in the HU to material conversion are required. This will be addressed in  
43 future work.

44 We follow the current practice by assigning human tissue parameters to mouse  
45 tissues, which will lead to further inaccuracies in small animal treatments.<sup>32</sup> Only very  
46 limited data on mouse tissue composition is currently available. Once more data on  
47 mouse tissues is available, further analysis of the number and choice of materials for the  
48 pre-calculated kernels and the HU to material conversion will be necessary.

49 Our dose engine is implemented on a multi-core CPU environment and has been  
50 optimized for calculation speed. Calculation times for a (5mm)<sup>2</sup> field single-beam plan in  
51 the water phantom are 5.2s, and 18s for a five-beam irradiation on a mouse CBCT. The  
52 dose calculation in Muriplan for the same treatment plans required 5.4s and 18s  
53 respectively. Halving the size of the zero-padding has significantly reduced the  
54 calculation times without reducing calculation accuracy. Based on these results we will  
55  
56  
57  
58  
59  
60  
61  
62  
63  
64  
65

1 implement a smart padding, which chooses the smallest possible zero-padding without  
2 compromising the accuracy based on the CT and beam plan, to reduce the calculation  
3 times further.

4 Kernel-based approaches generally come with a loss of accuracy compared to full MC  
5 simulations, but offer faster computation times. The commercial treatment planning  
6 system SmARTplan (SmART scientific solutions B.V., Maastricht, NL) employs a MC dose  
7 engine. Dose calculation times of 243s have been reported for an irradiation of the left  
8 kidney of a rat with four (1cm)<sup>2</sup> beams.<sup>17</sup> In addition, MC dose calculations are generally  
9 performed for a specific statistical uncertainty in the target region. While this avoids an  
10 increase in computation times with the number of treatment beams, it results in a loss of  
11 statistics in low dose regions. Our dose engine is a fast alternative to general full MC  
12 simulations with an acceptable accuracy, and it is promising for the use in an inverse  
13 treatment planning environment.  
14

## 15 16 17 V. CONCLUSIONS 18

19 We have presented a dose calculation engine for small animal radiotherapy, which is  
20 based on a superposition-convolution approach adapted to kV photon beams. Good  
21 agreement of the calculated dose distributions with Monte Carlo simulations could be  
22 shown in water, in slab phantoms and for a mouse CBCT. Runtimes are in the order of 5s  
23 for a single beam. Future work will focus on the energy and material sampling points, as  
24 well as improvements to the head model and the adaptation of input parameters of our  
25 dose algorithm to the treatment device. We believe the presented dose calculation  
26 algorithm will be valuable in inverse treatment plan optimization, which we identify as  
27 one of the main steps to further advance high-precision small animal radiotherapy.  
28  
29  
30  
31  
32  
33  
34  
35  
36  
37  
38  
39  
40  
41  
42  
43  
44  
45  
46  
47  
48  
49  
50  
51  
52  
53  
54  
55  
56  
57  
58  
59  
60  
61  
62  
63  
64  
65

- 1 Butterworth KT, Prise KM, Verhaegen F. Small animal image-guided radiotherapy: status, considerations and potential for translational impact. *The British Journal of Radiology*. 2015;88(1045):20140634.
- 2 Wong J, Armour E, Kazanzides P, Iordachita I, Tryggstad E, Deng H, et al. High-resolution, small animal radiation research platform with x-ray tomographic guidance capabilities. *International journal of radiation oncology, biology, physics*. 2008 Aug;71(5):1591–9.
- 3 Zhou H, Ph D, Rodriguez M, Haak FVD, Nelson G, Xu J, et al. Development of a MicroCT-Based Image-Guided Conformal Radiotherapy System for Small Animals. *Int J Radiat Oncol Biol Phys*. 2010;78(1):297–305.
- 4 Clarkson R, Lindsay PE, Ansell S, Wilson G, Jelveh S, Hill RP, et al. Characterization of image quality and image-guidance performance of a preclinical microirradiator. *Medical Physics*. 2011;38(2):845.
- 5 Stojadinovic S, Low Da, Hope aJ, Vicic M, Deasy JO, Cui J, et al. MicroRTsmall animal conformal irradiator. *Medical Physics*. 2007;34(12):4706.
- 6 Tillner F, Thute P, L'ock S, Dietrich A, Fursov A, Haase R, et al. Precise image-guided irradiation of small animals: a flexible non-profit platform. *Physics in Medicine and Biology*. 2016;61(8):3084–3108.
- 7 Verhaegen F, Granton P, Tryggstad E. Small animal radiotherapy research platforms. *Physics in Medicine and Biology*. 2011 Jun;56(12):R55–83.
- 8 Bazalova M, Nelson G, Noll JM, Graves EE. Modality comparison for small animal radiotherapy: a simulation study. *Medical physics*. 2014 Jan;41(1):011710.
- 9 Verhaegen F, van Hoof S, Granton PV, Trani D. A review of treatment planning for precision image-guided photon beam pre-clinical animal radiation studies. *Zeitschrift fur medizinische Physik*. 2014 Mar;.
- 10 Marco-Rius I, Wack L, Tsiamas P, Tryggstad E, Berbeco R, Hesser J, et al. A fast analytic dose calculation method for arc treatments for kilovoltage small animal irradiators. *Physica medica*. 2013 Sep;29(5):426–35.
- 11 Jacques R, Smith D, Tryggstad E, Wong J. GPU accelerated real time kV/MV dose computation. *Proc ICCR 2010*. 2010;p. 2–5.
- 12 Jacques R, Taylor R, Wong J, McNutt T. Towards real-time radiation therapy: GPU accelerated superposition/convolution. *Computer methods and programs in biomedicine*. 2010 jun;98(3):285–92.
- 13 Jacques R, Wong J, Taylor R, McNutt T. Real-time dose computation: GPU-accelerated source modeling and superposition/convolution. *Medical physics*. 2011;38(1):294–305.
- 14 Chow JCL, Leung MKK. Treatment planning for a small animal using Monte Carlo simulation. *Medical Physics*. 2007;34(12):4810.
- 15 Graves EE, Zhou H, Chatterjee R, Keall PJ, Gambhir SS, Contag CH, et al. Design and evaluation of a variable aperture collimator for conformal radiotherapy of small animals using a microCT scanner. *Medical Physics*. 2007;34(11):4359.
- 16 van Hoof SJ, Granton PV, Verhaegen F. Development and validation of a treatment planning system for small animal radiotherapy: SmART-Plan. *Radiotherapy and oncology : journal of the European Society for Therapeutic Radiology and Oncology*. 2013 Dec;109(3):361–6.
- 17 Balvert M, van Hoof SJ, Granton PV, Trani D, den Hertog D, Hoffmann AL, et al. A framework for inverse planning of beam-on times for 3D small animal radiotherapy using interactive multi-objective optimisation. *Physics in Medicine and Biology*. 2015;60(14):5681–5698.
- 18 Bartzsch S. Microbeam Radiation Therapy physical and biological aspects of a new cancer therapy and development of a treatment planning system. PhD Thesis, University of Heidelberg, Germany; 2014.
- 19 Bartzsch S, Oelfke U. A new concept of pencil beam dose calculation for 40-200 keV photons using analytical dose kernels. *Medical Physics*. 2013 Nov;40(11):111714.

- 1  
2  
3  
4  
5  
6  
7  
8  
9  
10  
11  
12  
13  
14  
15  
16  
17  
18  
19  
20  
21  
22  
23  
24  
25  
26  
27  
28  
29  
30  
31  
32  
33  
34  
35  
36  
37  
38  
39  
40  
41  
42  
43  
44  
45  
46  
47  
48  
49  
50  
51  
52  
53  
54  
55  
56  
57  
58  
59  
60  
61  
62  
63  
64  
65
- <sup>20</sup> Schneider W, Bortfeld T, Schlegel W. Correlation between CT numbers and tissue parameters needed for Monte Carlo simulations of clinical dose distributions. *Physics in Medicine and Biology*. 2000;45(2):459.
- <sup>21</sup> Agostinelli S, Allison J, Amako K, Apostolakis J, Araujo H, Arce P, et al. Geant4a simulation toolkit. *Nuclear Instruments and Methods in Physics Research Section A: Accelerators, Spectrometers, Detectors and Associated Equipment*. 2003;506(3):250 – 303.
- <sup>22</sup> Allison J, Amako K, Apostolakis J, Araujo H, Dubois P, Asai M, et al. Geant4 developments and applications. *IEEE Transactions on Nuclear Science*. 2006;53:270–278.
- <sup>23</sup> Siddon RL. Fast calculation of the exact radiological path for a three-dimensional CT array. *Medical Physics*. 1985;12(2):252.
- <sup>24</sup> Siggel M, Ziegenhein P, Nill S, Oelfke U. Boosting runtime-performance of photon pencil beam algorithms for radiotherapy treatment planning. *Physica Medica*. 2012;28(4):273–280.
- <sup>25</sup> Granton PV, Verhaegen F. On the use of an analytic source model for dose calculations in precision image-guided small animal radiotherapy. *Physics in Medicine and Biology*. 2013 May;58(10):3377–95.
- <sup>26</sup> <https://software.intel.com/en-us/intel-mkl>.
- <sup>27</sup> Fedorov A, Beichel R, Kalpathy-Cramer J, Finet J, Fillion-Robin JC, Pujol S, et al. 3D Slicer as an Image Computing Platform for the Quantitative Imaging Network. *Magnetic Resonance Imaging*. 2012 11;30(9):1323–41.
- <sup>28</sup> Cho NB, Kazanzides P. A Treatment Planning System for the Small Animal Radiation Research Platform (SARRP) based on 3D Slicer. *MIDAS Journal*. 2012;p. 1–8. Available from: <http://hdl.handle.net/10380/3364>.
- <sup>29</sup> <http://physics.nist.gov/PhysRefData/XrayMassCoef/cover.html>.
- <sup>30</sup> ICRU. ICRU Report 44 1989 Tissue Substitutes in Radiation Dosimetry and Measurement. 1989;.
- <sup>31</sup> Personal communication with XStrahl. T. Kanesalingam. 15.08.2016.
- <sup>32</sup> Bazalova M, Graves EE. The importance of tissue segmentation for dose calculations for kilovoltage radiation therapy. *Medical Physics*. 2011;38(6):3039.
- <sup>33</sup> Tryggestad E, Armour M, Iordachita I, Verhaegen F, Wong JW. A comprehensive system for dosimetric commissioning and Monte Carlo validation for the small animal radiation research platform. *Physics in Medicine and Biology*. 2009 Sep;54(17):5341–57.
- <sup>34</sup> Personal communication with XStrahl. T. Kanesalingam. 11.10.2016.



List of figure legends:

FIG. 1: Workflow of the developed dose calculation algorithm.

FIG. 2: Comparison of the analytical dose engine with Muriplan and MC simulations in water. Depth dose curves (left column) and lateral profiles at a depth of 6mm (right column) are shown for three different field sizes ( $(1\text{mm})^2$  top row,  $(5\text{mm})^2$  middle row, and  $(10\text{mm})^2$  bottom row). The depth dose curves are normalized to the value at 2cm depth. The local percentage differences were smoothed with a 3-median filter to reduce the visual impact of MC noise.

FIG. 3: Comparison of the depth dose curves of  $(5\text{mm})^2$  fields, normalized to the value at 2cm depth, calculated with the analytical dose engine, Muriplan, and MC simulations in slab phantoms of soft tissue with bone (left) and lung (right) inserts. The local percentage differences, smoothed with a 3-median filter, are shown in the bottom row.

FIG. 4: Dose distributions from a five  $(3\text{mm})^2$  field irradiation calculated on a mouse CBCT using the new dose engine (a), MC simulations (b) and Muriplan (c). The absolute dose differences are shown in the bottom row.